












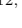





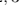







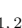























Pulse Profile Variability of PSR J1022+1001 in NANOGrav Data

WILLIAM FIORE ^{1,2,3} MAURA A. MCLAUGHLIN ^{2,3} GABRIELLA AGAZIE ⁴ AKASH ANUMARLAPUDI ⁴
ANNE M. ARCHIBALD ⁵ ZAVEN ARZOUMANIAN ⁶ PAUL T. BAKER ⁷ PAUL R. BROOK ⁸
H. THANKFUL CROMARTIE ⁹ KATHRYN CROWTER ¹ MEGAN E. DECESAR ¹⁰ PAUL B. DEMOREST ¹¹
LANKESWAR DEY ^{2,3} TIMOTHY DOLCH ^{12,13} ELIZABETH C. FERRARA ^{14,15,16} EMMANUEL FONSECA ^{2,3}
GABRIEL E. FREEDMAN ⁴ NATE GARVER-DANIELS ^{2,3} PETER A. GENTILE ^{2,3} JOSEPH GLASER ^{2,3}
DEBORAH C. GOOD ¹⁷ JEFFREY S. HAZBOUN ¹⁸ ROSS J. JENNINGS ^{2,3,*} MEGAN L. JONES ⁴
DAVID L. KAPLAN ⁴ MATTHEW KERR ¹⁹ MICHAEL T. LAM ^{20,21,22} DUNCAN R. LORIMER ^{2,3} JING LUO ^{23,†}
RYAN S. LYNCH ²⁴ ALEXANDER MCEWEN ⁴ NATASHA MCMANN ²⁵ BRADLEY W. MEYERS ^{1,26} CHERRY NG ²⁷
DAVID J. NICE ²⁸ TIMOTHY T. PENNUCCI ²⁹ BENETGE B. P. PERERA ³⁰ NIHAN S. POL ²⁵
HENRI A. RADOVAN ³¹ SCOTT M. RANSOM ³² PAUL S. RAY ¹⁹ ANN SCHMIEDEKAMP ³³ CARL SCHMIEDEKAMP ³³
BRENT J. SHAPIRO-ALBERT ^{2,3,34} INGRID H. STAIRS ¹ KEVIN STOVALL ¹¹ ABHIMANYU SUSOBHANAN ³⁵
JOSEPH K. SWIGGUM ^{28,*} AND HALEY M. WAHL ^{2,3}

¹Department of Physics and Astronomy, University of British Columbia, 6224 Agricultural Road, Vancouver, BC V6T 1Z1, Canada

²Department of Physics and Astronomy, West Virginia University, P.O. Box 6315, Morgantown, WV 26506, USA

³Center for Gravitational Waves and Cosmology, West Virginia University, Chestnut Ridge Research Building, Morgantown, WV 26505, USA

⁴Center for Gravitation, Cosmology and Astrophysics, Department of Physics, University of Wisconsin-Milwaukee, P.O. Box 413, Milwaukee, WI 53201, USA

⁵Newcastle University, NE1 7RU, UK

⁶X-Ray Astrophysics Laboratory, NASA Goddard Space Flight Center, Code 662, Greenbelt, MD 20771, USA

⁷Department of Physics and Astronomy, Widener University, One University Place, Chester, PA 19013, USA

⁸Institute for Gravitational Wave Astronomy and School of Physics and Astronomy, University of Birmingham, Edgbaston, Birmingham B15 2TT, UK

⁹National Research Council Research Associate, National Academy of Sciences, Washington, DC 20001, USA resident at Naval Research Laboratory, Washington, DC 20375, USA

¹⁰George Mason University, Fairfax, VA 22030, resident at the U.S. Naval Research Laboratory, Washington, DC 20375, USA

¹¹National Radio Astronomy Observatory, 1003 Lopezville Rd., Socorro, NM 87801, USA

¹²Department of Physics, Hillsdale College, 33 E. College Street, Hillsdale, MI 49242, USA

¹³Eureka Scientific, 2452 Delmer Street, Suite 100, Oakland, CA 94602-3017, USA

¹⁴Department of Astronomy, University of Maryland, College Park, MD 20742, USA

¹⁵Center for Research and Exploration in Space Science and Technology, NASA/GSFC, Greenbelt, MD 20771

¹⁶NASA Goddard Space Flight Center, Greenbelt, MD 20771, USA

¹⁷Department of Physics and Astronomy, University of Montana, 32 Campus Drive, Missoula, MT 59812

¹⁸Department of Physics, Oregon State University, Corvallis, OR 97331, USA

¹⁹Space Science Division, Naval Research Laboratory, Washington, DC 20375-5352, USA

²⁰SETI Institute, 339 N Bernardo Ave Suite 200, Mountain View, CA 94043, USA

²¹School of Physics and Astronomy, Rochester Institute of Technology, Rochester, NY 14623, USA

²²Laboratory for Multiwavelength Astrophysics, Rochester Institute of Technology, Rochester, NY 14623, USA

²³Department of Astronomy & Astrophysics, University of Toronto, 50 Saint George Street, Toronto, ON M5S 3H4, Canada

²⁴Green Bank Observatory, P.O. Box 2, Green Bank, WV 24944, USA

²⁵Department of Physics and Astronomy, Vanderbilt University, 2301 Vanderbilt Place, Nashville, TN 37235, USA

²⁶International Centre for Radio Astronomy Research, Curtin University, Bentley, WA 6102, Australia

²⁷Dunlap Institute for Astronomy and Astrophysics, University of Toronto, 50 St. George St., Toronto, ON M5S 3H4, Canada

²⁸Department of Physics, Lafayette College, Easton, PA 18042, USA

²⁹Institute of Physics and Astronomy, Eötvös Loránd University, Pázmány P. s. 1/A, 1117 Budapest, Hungary

³⁰Arecibo Observatory, HC3 Box 53995, Arecibo, PR 00612, USA

³¹Department of Physics, University of Puerto Rico, Mayagüez, PR 00681, USA

³²*National Radio Astronomy Observatory, 520 Edgemont Road, Charlottesville, VA 22903, USA*

³³*Department of Physics, Penn State Abington, Abington, PA 19001, USA*

³⁴*Giant Army, 915A 17th Ave, Seattle WA 98122*

³⁵*Max-Planck-Institut für Gravitationsphysik (Albert-Einstein-Institut), Callinstrasse 38, D-30167, Hannover, Germany*

ABSTRACT

Pulse profile stability is a central assumption of standard pulsar timing methods. Thus, it is important for pulsar timing array experiments such as the North American Nanohertz Observatory for Gravitational Waves (NANOGrav) to account for any pulse profile variability present in their data sets. We show that in the NANOGrav 15-yr data set, the integrated pulse profile of PSR J1022+1001 as seen by the Arecibo radio telescope at 430, 1380, and 2030 MHz varies considerably in its shape from observation to observation. We investigate the possibility that this is due to the “ideal feed assumption” (IFA), on which NANOGrav’s routine polarization calibration procedure relies. PSR J1022+1001 is $\sim 90\%$ polarized in one pulse profile component, and also has significant levels of circular polarization. Time-dependent deviations in the feed’s polarimetric response (PR) could cause mixing between the intensity I and the other Stokes parameters, leading to the observed variability. We calibrate the PR using a mixture of Measurement Equation Modeling and Measurement Equation Template Matching techniques. The resulting profiles are no less variable than those calibrated using the IFA method, nor do they provide an improvement in the timing quality of this pulsar. We observe the pulse shape in 25-MHz bandwidths to vary consistently across the band, which cannot be explained by interstellar scintillation in combination with profile evolution with frequency. Instead, we favor phenomena intrinsic to the pulsar as the cause.

1. INTRODUCTION

In 2023, pulsar timing array (PTA; Foster & Backer 1990) collaborations around the world released data sets presenting evidence of a stochastic background of gravitational waves (GWs) at \sim nanohertz frequencies (Agazie et al. 2023a; Antoniadis et al. 2023a; Reardon et al. 2023; Xu et al. 2023). For the past several years, these ongoing experiments have regularly observed dozens of radio pulsars in our Galaxy, in an effort to detect and characterize the properties of this GW background (GWB), determine the source(s) of the GWB, and detect continuous GWs from inspiraling supermassive black hole binaries. The North American Nanohertz Observatory for Gravitational Waves (NANOGrav; Ransom et al. 2019) is one such collaboration, and its most recent data release is the 15-yr data set (Agazie et al. 2023b, hereafter NG15).

The regular rotations of pulsars, when paired with regular (\sim monthly) observations over a span of months to years, allow us to unambiguously account for each rotation of the neutron star. This is achieved by constructing a *timing model*, which is composed of any and all parameters that measurably impact the times of arrival (TOAs) of the pulsar signal at the telescope. This includes (but is not limited to) rotational, astrometric,

and binary (if applicable) parameters. The TOAs predicted by the model are subtracted from those measured by observation to obtain timing *residuals*, which are used to refine the timing model.

A GW signal arises in PTA data as a red noise process in the timing residuals, and should be correlated between the pulsars in a characteristic way (Agazie et al. 2023a). It is, then, critically important to characterize all sources of noise and systematic error in pulsar timing residuals, so as not to confuse noise of non-GW origin for a detection, and maintain the best sensitivity to GWs (Agazie et al. 2023c). Thus, it is important to investigate any unusual behavior by a pulsar in a PTA data set that could potentially give rise to unaccounted-for noise.

1.1. PSR J1022+1001

PSR J1022+1001, is an MSP with $P = 16.45$ ms and a dispersion measure (DM) of 10.26 pc cm^{-3} , in a 7.8 day orbit with a white dwarf companion (Camilo et al. 1996). It is observed by the European Pulsar Timing Array (EPTA; Antoniadis et al. 2023b), Parkes Pulsar Timing Array (PPTA; Zic et al. 2023), and NANOGrav. Since shortly after its discovery, PSR J1022+1001 has been known to exhibit strange pulse shape variations from observation to observation (Camilo et al. 1996; Kramer et al. 1999). This is illustrated in Figure 1, which shows integrated pulse profiles obtained from two NANOGrav observations of PSR J1022+1001 with the 305-m radio

* NANOGrav Physics Frontiers Center Postdoctoral Fellow

† Deceased

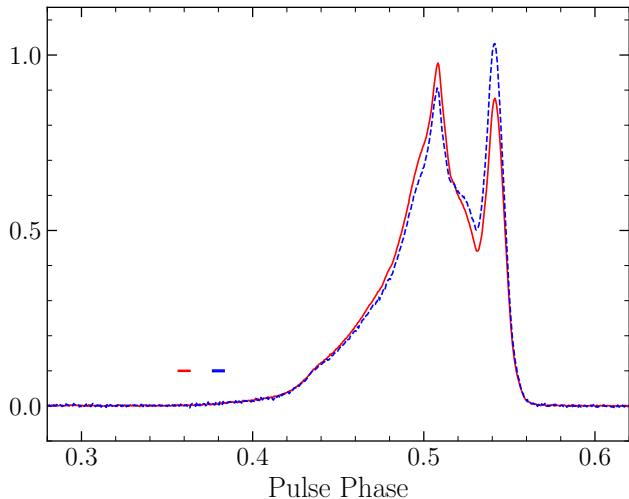


Figure 1. Two example pulse profiles of PSR J1022+1001 from 1.4-GHz Arecibo observations in the NANOGrav 15-yr data set. The solid red profile corresponds to an observation made on 5 November 2015, while the dashed blue profile was obtained on 5 April 2020; these observations were chosen to illustrate the stark difference in peak heights between the two pulse profiles. The profiles were normalized using the area under the curve. The pulse phase is given in units of rotations. The small red and blue “lines” in the bottom left of the figure are actually error bars showing the level of off-pulse noise in each profile.

telescope at the Arecibo Observatory (AO), one of which was performed 4.4 yr after the other. A clear difference in the pulse shape can be seen, such that the first peak is higher than the second in one case, while the reverse is true in the other. This variability has been studied over nearly three decades, with contradictory conclusions as to the underlying cause, or whether there is even variability at all (Kramer et al. 1999; Ramachandran & Kramer 2003; Hotan et al. 2004; van Straten 2013; Liu et al. 2015; Shao & You 2016; Padmanabh et al. 2021).

When pulsar data are folded over several thousand rotations, the resulting pulse profile is generally long-term stable, as the fluctuations in the shapes of individual pulses average out (this stability is, however, limited by pulse jitter; Lam et al. 2019). However, integrated pulse profiles have been observed to vary in some pulsars due to various causes. Some pulsars exhibit forms of pulse shape variability such as *mode changing*, where on timescales of several to thousands of rotations, the pulse profile changes between two or more distinct shapes (Backer 1970; Wang et al. 2007). Pulse profiles have also been seen to change over time for binary pulsars due to geodetic precession (e.g. Cameron et al. 2023).

In the case of PSR J1713+0747, a sudden change was observed in the pulse profile, which then gradually ap-

proached its previous shape over the course of several months (Jennings et al. 2024). Geodetic precession was ruled out as a cause, but an extreme case of mode changing was not. Other proposed causes include plasma lensing in the ISM (not ruled out), a shape change associated with a glitch (ruled out), and more exotic phenomena such as the incursion of an asteroid into the pulsar magnetosphere. While there is no single satisfying explanation, some event related to the pulsar magnetosphere seems most likely (Jennings et al. 2024).

The profile variability seen for PSR J1022+1001 does not fit neatly into any of the above categories. It is seemingly random, without any distinct modes or long-term trends (Kramer et al. 1999). Notably, PSR J1022+1001’s pulse profile is highly polarized, with the polarization fraction reaching $\sim 90\%$ in the second peak of emission. Thus, one hypothesized cause of the observed phenomenon is mixing between polarized and unpolarized intensities caused by polarization miscalibration (Kramer et al. 1999; van Straten 2013). The main purpose of this paper is to use NANOGrav timing observations to evaluate the likelihood of this possibility.

1.2. Pulsar Polarimetry

The intensity of a polarized electromagnetic wave is described by the Stokes vector

$$\mathbf{S} = \begin{bmatrix} I \\ Q \\ U \\ V \end{bmatrix}, \quad (1)$$

where I is the total intensity, Q and U represent two orthogonal components of linearly-polarized emission, and V is the circularly-polarized intensity. The linearly-polarized intensity is given by $L = \sqrt{Q^2 + U^2}$, and the polarization angle (Ψ or P.A.) is given by

$$\Psi = 0.5 \tan^{-1} \left(\frac{U}{Q} \right). \quad (2)$$

In this work, we employ the IAU convention for P.A. and V , where $\Psi = 0^\circ$ points north, P.A. increases in the counter-clockwise direction, and $V > 0$ represents a rotation that increases the P.A. (a right-handed circularly polarized signal).

In the context of pulsars, the dependence of Ψ on pulse longitude φ is used to glean insights into the emission geometry. Especially in slow pulsars, Ψ often follows an “S”-shaped curve. This is explained by the Rotating Vector Model (RVM; Radhakrishnan & Cooke 1969), which has Ψ determined by the projection of the pulsar’s

magnetic field lines along the line of sight:

$$\tan(\Psi - \Psi_0) = \frac{\sin \alpha \sin(\varphi - \varphi_0)}{\sin \zeta \cos \alpha - \cos \zeta \sin \alpha \cos(\varphi - \varphi_0)}, \quad (3)$$

where Ψ_0 and φ_0 are values of Ψ and φ where the gradient of Ψ is greatest, defining the point of symmetry for the curve such that the pulsar beam is pointing most directly towards the observer; α is the angle between the pulsar's axis of rotation and the magnetic pole; and ζ is the angle between the rotation axis and the line of sight (Everett & Weisberg 2001). Therefore, the minimum angle between the magnetic axis and the line of sight is

$$\beta = \zeta - \alpha. \quad (4)$$

The P.A. recorded by a telescope on Earth must be corrected for Faraday rotation to obtain the true P.A. of the emitted signal. The component of the magnetic field along the line of sight to the pulsar, $B_{||}$, subjects the emission's P.A. to a wavelength-dependent rotation:

$$\Psi(\lambda) - \Psi_\infty = \text{RM} \lambda^2, \quad (5)$$

where Ψ_∞ is the P.A. at infinite frequency, λ is the wavelength of the radio waves and RM is the rotation measure, which is given (in Gaussian cgs units) by

$$\text{RM} = \frac{e^3}{2\pi m_e^2 c^4} \int_0^d n_e(l) B_{||}(l) dl \quad (6)$$

where n_e is the density of free electrons, e and m_e are the charge and mass of the electron, respectively, c is the speed of light, and d is the pulsar distance (Lorimer & Kramer 2004).

After correcting for Faraday rotation, the Stokes vector emitted by a polarized radio source ($\mathbf{S}_{\text{emitted}}$) differs from that which is recorded by a radio telescope (\mathbf{S}_{meas}) by a linear transformation:

$$\mathbf{S}_{\text{meas}} = \mathbf{M} \mathbf{S}_{\text{emitted}}. \quad (7)$$

Here, the Mueller matrix \mathbf{M} is effectively the transfer function for \mathbf{S} (Heiles et al. 2001), also known as the polarimetric response (PR) of the feed. We parameterize the PR as in Equation 18 of van Straten (2004), with the absolute gain G , differential gain γ , differential phase ϕ , and the orientations θ_k and ellipticities ϵ_k of receptors $k \in 0, 1$.

These parameters, which correspond to physical qualities of the feed, describe mixing between the components of \mathbf{S} . For example, assuming a linear feed, γ describes mixing between I and Q , while ϕ describes rotation about the Q axis. They are known to vary with time (e.g. Gentile et al. 2018), which could in turn cause \mathbf{S}_{meas} to vary with time even if $\mathbf{S}_{\text{emitted}}$ is stable.

In this work, we present the pulse profile variability seen in NANOGrav observations of PSR J1022+1001, and investigate whether robust polarization calibration can account for the observed variability. Observations of PSR J1022+1001 and the pulsars used for polarization calibration purposes are described in §2. Our methods of data reduction, polarization calibration, and pulsar timing are detailed in §3. We show our results in §4. Finally, we discuss our results in context of prior work and conclude with §5.

2. OBSERVATIONS

This work makes use of a subset of observations released as part of NG15, along with several observations of the slow pulsar B0525+21 (J0528+2200). Without exception, these data were taken at AO using the Puerto Rican Ultimate Pulsar Processing Instrument (PUPPI Van Rooy et al. 2017), which is a clone of the Green Bank Ultimate Pulsar Processing Instrument (GUPPI), the pulsar backend formerly used by the Green Bank Telescope (Ransom et al. 2009).

Observations were made with the 430 (circular feeds; 421–445 MHz bandwidth split into 1.5625-MHz wide frequency channels), L-wide (linear feeds; 1147–1765 MHz; 12.5 MHz channels) and S-wide (linear feeds; contiguous bands at 1700–1880 and 2050–2404 MHz; 12.5 MHz channels) receivers. The data were coherently folded and de-dispersed using the pulsar ephemerides, resulting in 10 s sub-integrations and 2048 pulse phase bins. We generally refer to the data using the approximate center frequencies instead of the receiver names: 430 MHz, 1.4 GHz, and 2 GHz data for the 430, L-wide, and S-wide receivers, respectively.

For a detailed description of NANOGrav timing observations and the 15-yr data set, see NG15. For our analysis, we used all AO observations of PSR J1022+1001 as our primary data of interest. PSR J1022+1001 was observed at AO 84 times between MJDs 57028 and 59055 (a ≈ 24 -day cadence). On each observing epoch, the pulsar was observed at both 430 MHz and 1.4 GHz (until MJD 57502) or 1.4 and 2 GHz (beginning MJD 57522) for about 20–25 min with each receiver.

For polarization calibration purposes (described in §3.1.3), we also made use of all 430-MHz observations of PSR J0030+0451 and all 1.4-GHz and 2-GHz observations of PSR B1937+21 (J1939+2134). Table 1 provides a summary of the observations of PSR B0525+21, which were not part of the NANOGrav 15-yr data release. These observations were purely for polarization calibration purposes, which are described in §3.1.2.

Data taken between 2017 August and 2018 November were affected by a malfunctioning local oscillator (LO)

Table 1. Observations of PSR B0525+21

Rcvr	ν	$\Delta\nu_{\text{usable}}$	$\Delta\nu_{\text{chan}}$	MJD	N_{obs}	t_{int}	Span
	(GHz)	(MHz)	(MHz)			(min)	(min)
430	0.43	24	1.5625	56744	4	75.5	129.3
L-wide	1.4	600	12.5	56116	3	56.2	109.3
S-wide	2.0	460	12.5	56116	3	31.4	112.7

NOTE—Summary of observations of PSR B0525+21 used to generate MEM receiver solutions. From left to right, columns correspond to receiver name, approximate center frequency, usable bandwidth, frequency channel bandwidth, MJD of the observations, number of observations, cumulative length of observations, and timespan between the start of the first observation and the end of the last observation. Aside from the total integration time, these observing setups are identical to those used by NANOGrav timing observations with these receivers.

at AO. This issue is described in further detail by NG15. As in that work, we disregarded all observations that fell within this time range.

3. METHODS

In §3.1, we describe the methods used to produce polarization-calibrated profiles. In §3.2, we describe our data reduction procedure and timing analysis of the calibrated data.

3.1. Polarization Calibration

In order to calibrate our observations of PSR J1022+1001, we used a combination of Measurement Equation Modeling (MEM; van Straten 2004) and Measurement Equation Template Matching (METM; van Straten 2013) methods. For a given receiver, we applied MEM to observations of the slow pulsar B0525+21 to produce a PR. Then, METM was used to calculate “corrections” to this PR using observations of “template pulsars” made on different epochs. The MEM PR, along with METM corrections, were then used to calibrate the observations of PSR J1022+1001.

In §3.1.1, we first describe the usual method of polarization calibration employed in NANOGrav data reduction, which is known as the “Ideal Feed Assumption,” or IFA. Then, we describe the process of generating receiver solutions using MEM (§3.1.2) and METM (§3.1.3). In each case, the data were calibrated using PSRCHIVE¹ (van Straten et al. 2011), in particular `pac`. In the cases of MEM and METM, `pcm` was first used in concert with calibration observations to generate PRs.

¹ <http://psrchive.sourceforge.net/>

3.1.1. Ideal Feed Assumption

The standard method of polarization calibration for NANOGrav timing observations aims to account for differences in gain and phase between the two receptors by observing a reference signal of artificial origin. A noise diode coupled to the receiver injects a polarized square wave signal of known amplitude and position angle, which is used to determine the absolute gain G , differential gain γ , and differential phase ϕ of the receptors. Approximately once per month, flux calibration is performed by measuring the noise diode signal simultaneously with on/off observations of a quasar (J1445+0958) whose emission is unpolarized and of a known flux density, which calibrates the amplitude of the reference signal and refines the determination of G .

This method assumes the receptors are perfectly orthogonal, the noise diode signal is 100% linearly polarized, and that it illuminates both receptors equally and in phase. However, flux calibration removes the need to assume the signal illuminates the receptors equally (van Straten 2002).

If the receptors are not perfectly orthogonal, the resulting cross-coupling between the two polarizations causes mixing between total intensity and polarized signal. For a highly-polarized pulsar signal, this could lead to a temporal variation in the total intensity pulse profile, as is seen for PSR J1022+1001 (van Straten 2013).

3.1.2. Measurement Equation Modeling

MEM uses one or multiple observations of a suitably-polarized pulsar that span a range of parallactic angles, along with an artificial noise diode signal (as with IFA), to fully characterize the PR of the receiver without requiring the assumptions made in IFA calibration. A first guess of the PR is obtained using the noise diode observation. A set of pulse phase bins are then chosen to model the dependency of the Stokes parameters on parallactic angle. These curves are then fitted to the polarization measurement equation (Hamaker 2000), and the best-fit solution gives the PR in the chosen parameterization. A flux calibrator observation (as described in Section 3.1.1) is used to break measurement equation degeneracy by constraining the mixing of Stokes I and either Q (for a linear feed) or V (for a circular feed). MEM is described in complete detail in van Straten (2004).

One MEM receiver solution was obtained for each receiver using observations of the slow pulsar B0525+21. These observations are described in Table 1. The resulting PR for the L-wide receiver (for MJD 56116) is shown in Figure 2.

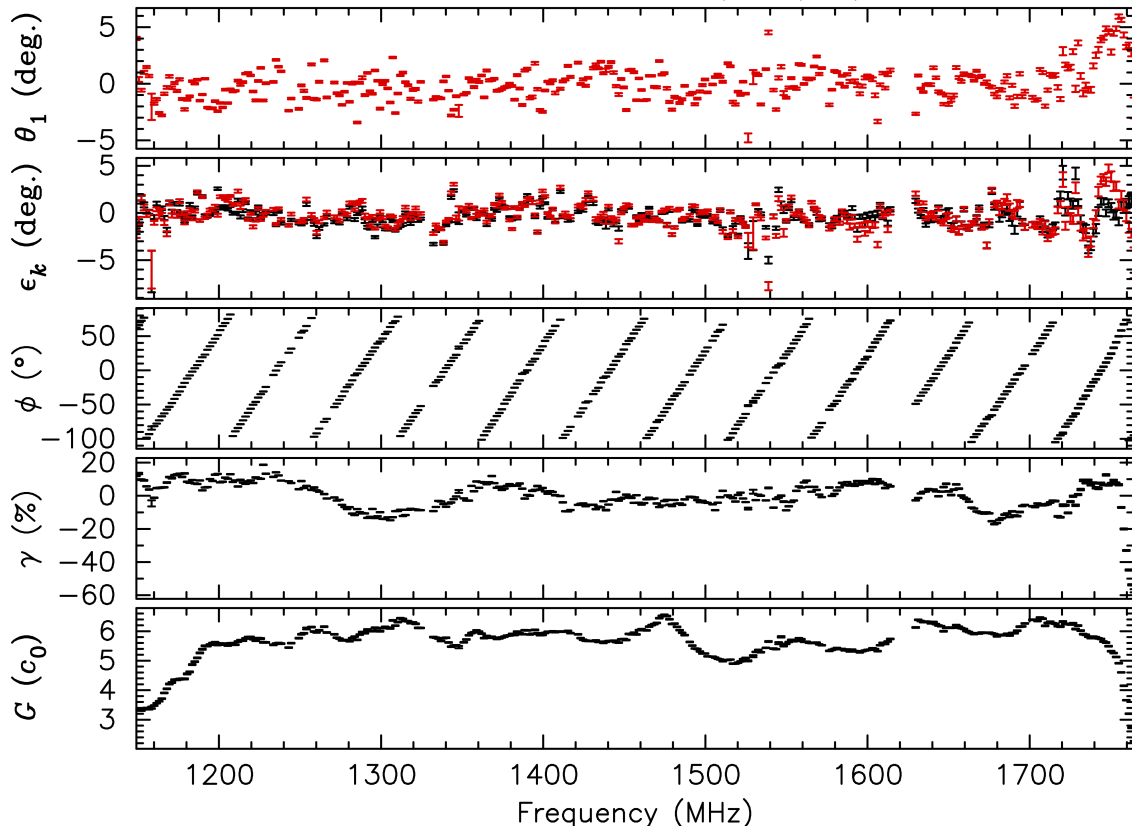


Figure 2. Polarimetric response of the L-wide (1.4 GHz) receiver on 7 August 2012 (MJD 56116). The parameters shown are θ_1 , the orientation of receptor 1 with respect to receptor 0; ϵ_k , the ellipticities of the receptors (receptor 0 in black and receptor 1 in red); ϕ , the differential phase; γ , the differential gain; and G , the absolute gain.

3.1.3. Measurement Equation Template Matching

METM calibration compares observations of a pulsar to a single calibrated “template” profile of the same pulsar, obtaining PRs on multiple epochs. Assuming the profile of this pulsar does not change with time, the PR is calculated by matching the profile in question to the template profile. This process is described fully in van Straten (2013).

We used PSRs J0030+0451 (at 430 MHz) and B1937+21 (at 1.4 and 2 GHz) as our template pulsars. These pulsars were chosen for their high S/N and significant levels of linear and circular polarization. Following Gentile et al. (2018), we apply the MEM PR to each observation of these pulsars. For each receiver, we first considered the two MEM-calibrated profiles taken closest in time to the MEM PR. In each case, these were visually indistinguishable from previously-published calibrated profiles in Gentile et al. (2018) and Wahl et al. (2022). From those two profiles, we chose the profile with the highest S/N to be our template profile. These were then used as described above, to create PRs corresponding to

each other template pulsar observation. These PRs can be thought of as corrections to the MEM PR, and were applied to the data of interest after first applying the MEM PR. An example METM PR is shown in Figure 3.

Interstellar scintillation induces a frequency-dependent flux density modulation on a timescale specific to each pulsar. When comparing observations of our template pulsars to the relevant template profile, differences in the flux density in each channel due to scintillation are covariant with changes in G . To avoid this, we normalized the Stokes parameters by the invariant interval $I^2 - Q^2 - U^2 - V^2$ (Britton 2000), trusting that G is sufficiently characterized by our flux calibrator observations.

3.2. Data Reduction & Timing Analysis

We largely followed the standard NANOGrav data reduction and TOA generation procedure, as described in NG15. First, data affected by the LO issue described in §2 were excluded. Artifacts introduced by the interleaved analog-to-digital converter scheme used by the PUPPI receiver (Alam et al. 2021) were removed

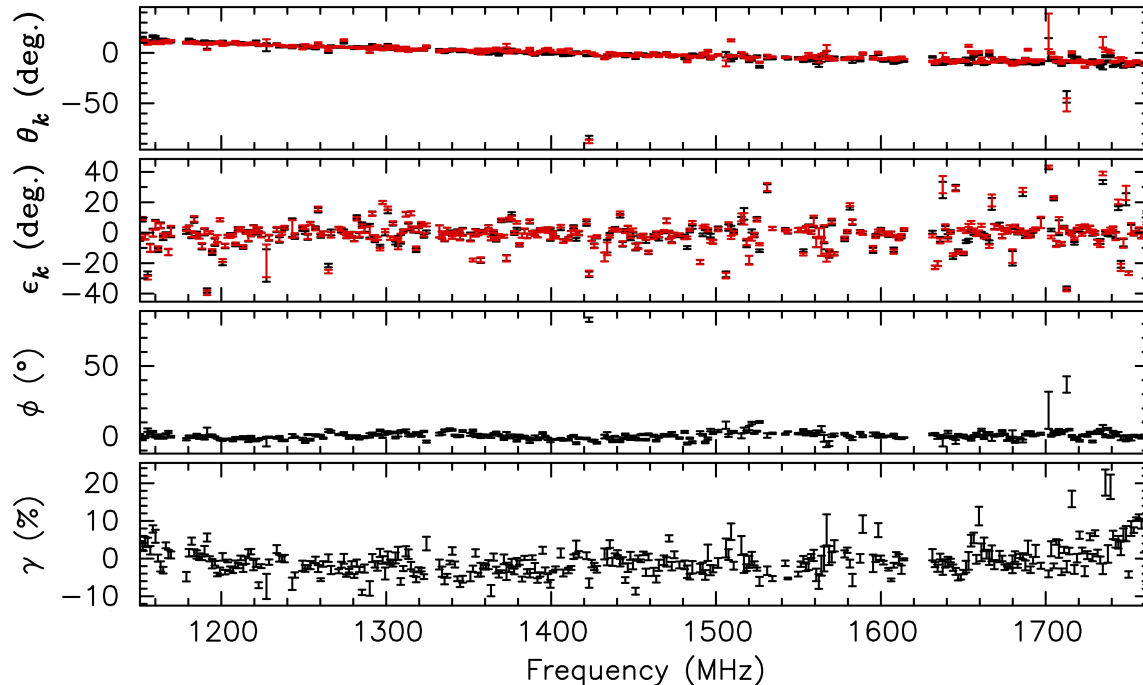


Figure 3. METM correction to the 1.4-GHz MEM PR calculated from a 31 July 2012 (MJD 56139) observation of PSR B1937+21. The parameters shown are the orientations θ_k and ellipticities ϵ_k of the receptors (receptor 0 in black and receptor 1 in red); ϕ , the differential phase; and γ , the differential gain. Because the Stokes parameters were normalized by the mean invariant, our METM solutions do not provide any information about the absolute gain G .

from the raw data. Then, we performed standard radio frequency interference (RFI) excision and polarization-calibrated the data as described above, followed by additional RFI excision. We performed the additional step of correcting the calibrated profiles for interstellar (and ionospheric) Faraday rotation using `rmfit`, assigning an RM to each observation. This was followed by time-averaging to maximum sub-integrations of 30 min, and (for 1.4 and 2 GHz data) frequency-averaging, achieving 12.5 MHz-wide subbands (430-MHz data kept the 1.5625 MHz-wide subbands of the raw data).

Following this, a standard template profile was created for each receiver by iteratively fitting a number of Gaussian curves to the S/N-weighted sum of the individual profiles. This Gaussian-based standard profile was then denoised with UD8 wavelet smoothing. TOAs were generated with `pat`, with a separate TOA being generated for each sub-integration and frequency subband by measuring the time shift between the profile and the template (Taylor 1992).

We then performed an outlier analysis on the TOAs, using the automated pipeline described in Section 3.3 of NG15. TOAs were removed if the pipeline determined an outlier probability greater than 0.1, or if the profile S/N was less than 8. Observations with $>8\%$ of

TOAs flagged as outliers were removed entirely. Observations where the ratio of maximum to minimum TOA frequency did not exceed 1.1 were also eliminated.

After outlier excision, we used `PINT_Pa1`,² the timing analysis package that was employed in NG15 and makes use of the pulsar timing package `PINT`³ (Luo et al. 2021; Susobhanan et al. 2024), to produce a timing solution. The timing parameters and TOAs are contained within a `par` and `tim` file, respectively. `PINT`, and indeed all pulsar timing methods, subtracts measured TOAs from the TOAs predicted by the pulsar’s timing model to obtain the timing residuals. A least-squares fit is performed on the residuals to estimate the timing model parameters. The `PINT_Pa1` timing notebooks also allow for modeling the noise characteristics of the timing residuals, and perform statistical tests to determine whether any parameters should be added to or removed from the model.

Our timing analysis closely follows NG15 §4, which we summarize here. We model the pulsar’s rotation with spin frequency, phase, and frequency derivative.

² https://github.com/nanograv/pint_pal

³ <https://github.com/nanograv/PINT>

Five parameters account for the astrometric position and motion of the pulsar: ecliptic longitude and latitude, proper motion in each coordinate, and timing parallax. To model timing variations caused by the pulsar’s orbit with its binary companion, we used the DD binary model (Damour & Deruelle 1985). The five Keplerian parameters (orbital period, projected semimajor axis, eccentricity, and epoch and longitude of periastron) are always fit, along with the corresponding derivatives if significant. The above parameters are referenced to the midpoint of the data timespan.

Due to the turbulent ionized ISM and ionospheric and solar-wind variations, pulsar dispersion measures are time-dependent (Jones et al. 2017). To account for these variations, we employ the DMX model of time-dependent dispersion measure in PINT, which is a piecewise constant function. TOAs are divided into distinct epochs of a specified length, and each epoch is assigned a single DMX parameter. Each DMX parameter describes the offset between the measured DM within an epoch and a fixed reference DM.

Because of its low ecliptic latitude, our line of sight to PSR J1022+1001 annually intercepts the Sun. When the pulsar’s angular distance from the Sun is small, the solar wind induces timing variations exceeding 100 ns at all of our observing frequencies. Due to this, and the fact that observations were made at multiple frequencies on the same day at AO (enabling a precise measurement of DM from a single day’s observations), we follow Agazie et al. (2023b) in using DMX epochs of half-day length.

PSR J1022+1001’s pulse profile is noticeably frequency-dependent within the bandwidths of the receivers, especially that of the L-wide receiver. Differences between the shape of the standard profile and the profiles corresponding to the subbanded TOAs can induce frequency-dependent timing variations. In the timing analysis, we account for the effects of these variations using frequency-dependent (FD) parameters c_i (also FD1, FD2, etc.) that describe a timing delay

$$\Delta_{\text{FD}} = \sum_{i=1}^n c_i \log \left(\frac{\nu}{1 \text{ GHz}} \right)^i \quad (8)$$

(NANOGrav Collaboration et al. 2015).

Lastly, constant phase offsets between the different AO receivers were accounted for by fitting two JUMP parameters. We determined whether to add new timing model parameters or remove existing ones using a statistical F -test, including parameters only if $3\text{-}\sigma$ confidence was reached. For consistency with NANOGrav’s timing process, proper motion and parallax parameters were included regardless of significance (NG15).

When we began our timing analysis, we noted that the DM reported in the 15-yr `par` file (9.435 pc cm^{-3}) was significantly different from the value used for coherent dedispersion (10.26 pc cm^{-3}). From visual inspection of the data, it became clear that the 15-yr value was incorrect. We see similar discrepancies for other pulsars, such as a 0.08 pc cm^{-3} excess for PSR B1937+21. Further investigation showed this was due to a covariance between the DMX and FD parameters that led to the FD parameters absorbing a ν^{-2} delay, and biasing the DMX parameters. This bias was absorbed into the reference DM as part of NANOGrav’s iterative timing process, which sets the DMX parameters to have a mean value of zero with each iteration.

Efforts to avoid this problem in the future are underway within NANOGrav. In this analysis, we only added an FD parameter if doing so did not cause a large change ($\gtrsim 0.1 \text{ pc cm}^{-3}$) in the DMX average, which we interpret as spurious. We did not see the same phenomenon while performing our timing analysis on the calibrated profiles.

We also performed the outlier and timing analysis steps on the observations of PSR J1022+1001 as presented in NG15, which were only subjected to the standard IFA-based polarization calibration. This amounted to redoing the same analysis as in NG15, except we avoided adding FD parameters when this resulted in a significant departure from the known DM value, even if such an addition was preferred by F -tests. Hereafter, we refer our two data sets as the IFA and METM data sets.

4. RESULTS

In §4.2, we describe our analysis of profile variability in the IFA and METM data sets. In §4.3, we compare the timing solutions obtained from the IFA and METM data sets.

4.1. Polarization Profiles

Each METM-calibrated, RM-corrected profile was added in phase using `psradd` to produce average polarization profiles for each receiver. These are shown in Figures 4, 5, and 6, and the latter two include fitted RVM P.A. curves, described below.

In order to produce the 430-MHz profile shown in Figure 4, we first corrected a sign flip in the P.A. and Stokes- V curves, which were recorded as having the opposite sign of their L- and S-band counterparts. Considering the profiles of PSR J1022+1001 presented in Stairs et al. (1999), which were obtained at Jodrell Bank, we see that the corresponding curves are broadly consistent in shape from 410 to 1414 MHz (a downward-sloping P.A. curve near the pulse peaks and a negative peak for V). That

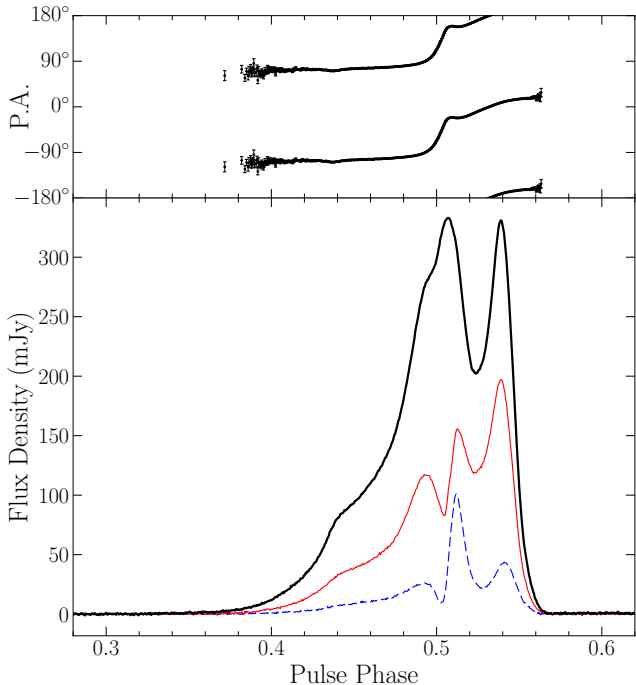


Figure 4. METM-calibrated polarization profile of PSR J1022+1001 at 430 MHz. The bottom panel shows the total intensity profile (Stokes I) with the thick black line, the linear polarization (L) with the thin red line, and the circular polarization (V) with the blue dashed line. The top panel shows the P.A. swing in bins for which $L > 3\sigma_I$. We used the IAU convention for P.A. and V .

work uses the opposite sign convention for P.A. and V from ours (P.A. increases clockwise and a left-handed signal has $V > 0$), and yet our 430-MHz P.A. and V curves match their 410-MHz data. It is apparent that Arecibo’s 430-MHz receiver used this convention during our observations, and this was not properly recorded in the PSRFITS file headers. We corrected for this error by flipping the signs of U and V .

RMs, mean flux densities, and pulse widths are given in Table 2. We used `ionFR`⁴, a package that estimates the ionospheric contribution to Faraday rotation (Sotomayor-Beltran et al. 2013), to ensure the reported RMs are purely astrophysical.

We applied the RVM (see Equation 3) to PSR J1022+1001’s P.A. curve, using the `psrmodel` routine in PSRCHIVE. Bins were only used for the fit if $L > 3\sigma_I$, where σ_I is the standard deviation in I . The resulting best-fit parameters are also presented in Table 2. We

⁴ <https://github.com/csobey/ionFR>

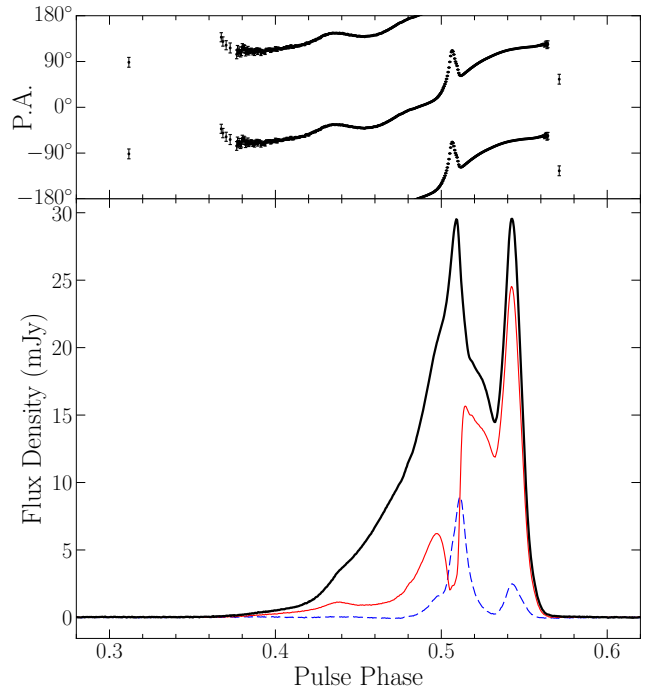


Figure 5. METM-calibrated polarization profile of PSR J1022+1001 at 1.4 GHz. See Figure 4’s caption for details. A Rotating Vector Model fit to the P.A. curve is also shown, and is described in the text.

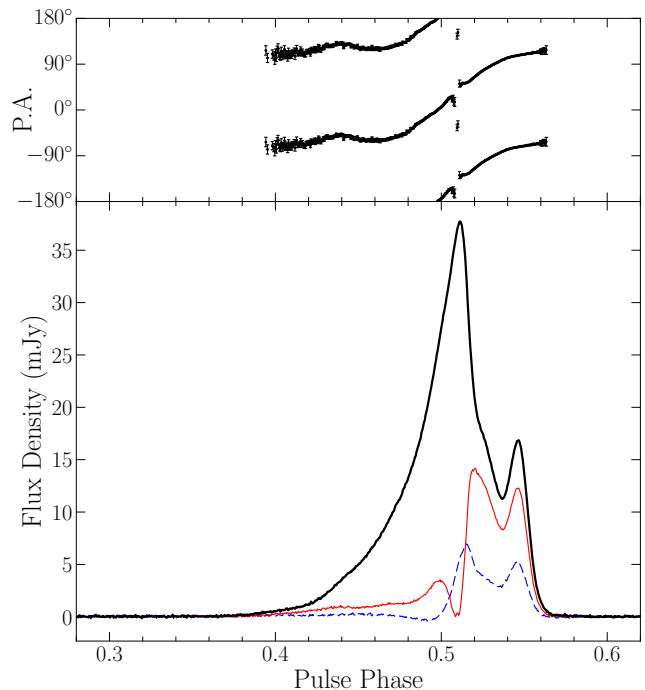


Figure 6. METM-calibrated polarization profile of PSR J1022+1001 at 2 GHz. See Figure 4’s caption for details. A Rotating Vector Model fit to the P.A. curve is also shown, and is described in the text.

Table 2. Rotation Measures, Flux Densities, Pulse Widths, and RVM Fits

Frequency	RM	Flux Density	W_{10}	W_{50}	φ_0^a	α	β	Reduced χ^2
(GHz)	(rad m^{-2})	(mJy)	(ms)	(ms)	($^\circ$)	($^\circ$)	($^\circ$)	
0.43	8(2)	25(16)	2.24	1.15
1.4	12(5)	2(3)	1.98	1.01	-1.09(2)	9(1)	-1.1(1)	1461
2.0	5(5)	2(3)	1.82	0.42	-0.405(8)	6(6)	-0.6(6)	201

^aRelative to phase of the leading peak of the profile.

NOTE—We report RMs, mean flux densities, and pulse widths at 10% and 50% peak intensity for calibrated profiles of PSR J1022+1001 at each frequency. The RMs shown are the interstellar RMs (calculated after accounting for ionospheric Faraday rotation). The uncertainties shown for RM and flux density are the epoch-to-epoch standard deviations. The other columns report best-fit RVM parameters given by PSRCHIVE’s `psrmodel` routine (along with the reported 1- σ uncertainties). See Equation 3 for a full description of the RVM parameters.

were unable to reach a convergent fit for the 430 MHz profile.

Neither the 1.4 or 2 GHz RVM fits are of particularly good quality, with very high reduced χ^2 . This is likely due, at least in part, to the “notch” seen in the P.A. curve near the phase when the beam is closest to the line of sight. The slope at this phase is used to estimate α and β :

$$\left. \frac{d\Psi}{d\varphi} \right|_{\varphi_0} = \frac{\sin \alpha}{\sin \beta}. \quad (9)$$

Stairs et al. (1999) were able to obtain a better RVM fit with their 1.4 GHz data from Jodrell Bank, finding $\alpha = 83(27)^\circ$ and $\beta = -7^\circ 1(4)$. Notably, their P.A. curve lacks the “notch” present in ours, but this could be simply due to a lack of points in the given phase range.

The poor quality of our RVM fits and their disagreement with prior studies suggests that despite the P.A. curve’s visual similarity to the well-behaved curves common for slower pulsars, PSR J1022+1001’s emission geometry is more complicated than what may be easily described by the RVM. One such complex geometry was explored by Ramachandran & Kramer (2003).

4.2. Pulse Profile Variability

Figures 7, 8, and 9 show the profile variability of both the IFA and METM data sets in the style of Hotan et al. (2004), with the modifications introduced in Padmanabh et al. (2021). We phase-aligned the profiles with `pas`, then normalized each profile by scaling it such that its integral is equal to unity (“flux-based normalization” in Hotan et al. 2004). In the normalization stage, profiles with S/N below a threshold value were removed: such profiles are problematic because their integral approaches zero. A S/N threshold was chosen separately for each receiver in order to balance keeping as many

profiles as possible with removing the noisiest few. For each receiver, we created a comparison profile by calculating the median value of the normalized profiles in each phase bin. Then, we created difference profiles by subtracting the median profile from the individual profiles on each epoch. We then quantified the variability by calculating the standard deviation of the difference profile values in each phase bin. In each data-set/receiver combination, these binned standard deviations are noticeably higher near the peaks of the pulse profile.

Another way to characterize the variability of the pulse profile is to compute the relative phases and heights of the two peaks that characterize PSR J1022+1001’s pulse profile. Following the ‘peak optimizer’ method presented by Padmanabh et al. (2021), we estimated each peak’s phase and height by fitting a parabola to the data within a certain number of bins of an initial guess of the peak phase bin. This guess was refined through multiple iterations.

The results of the peak optimizer fit are shown in Figure 10. We take the turning point of the best-fit parabola to be the phase of the peak, and the height of the polynomial to be the peak height. The best-fit phase differences and peak height ratios are plotted in Figures 11, 12, and 13.

We investigated whether the choice of calibration technique influenced the average pulse shape by performing a Kolmogorov-Smirnov test to compare the peak ratios of the IFA and METM data sets from each receiver. In each case, the test statistic does not indicate that the two data sets are drawn from different distributions. The lowest p -value was 0.54, for the 1.4 GHz data. As can be seen from Figure 14, there are certainly examples of IFA- and METM-calibrated data from the same

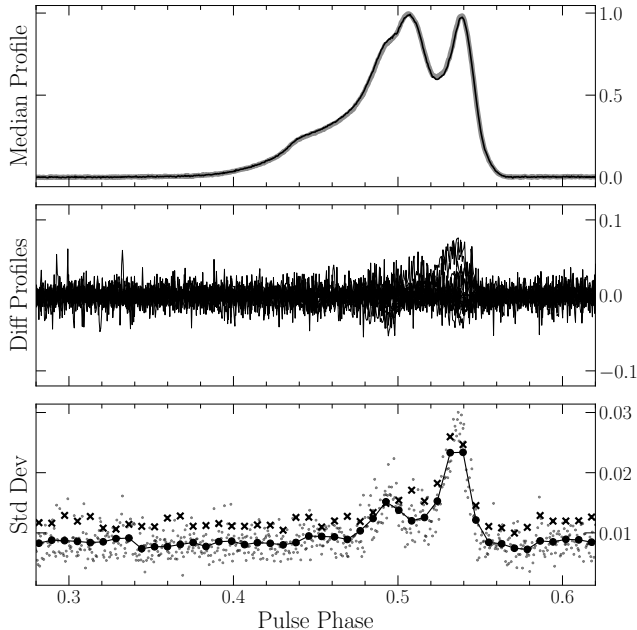


Figure 7. Profile variability visualization for 430 MHz data. The top panel shows median pulse profiles from IFA- (thick gray line) and METM-calibrated (thin black line) data, the middle panel shows METM-calibrated difference profiles (data subtracted by the median profile), and the bottom panel shows the binned standard deviation of the difference profiles (small grey points), as well as a moving average with only 128 bins (large black points). The moving average is also shown with ‘X’-shaped markers for IFA-calibrated data.

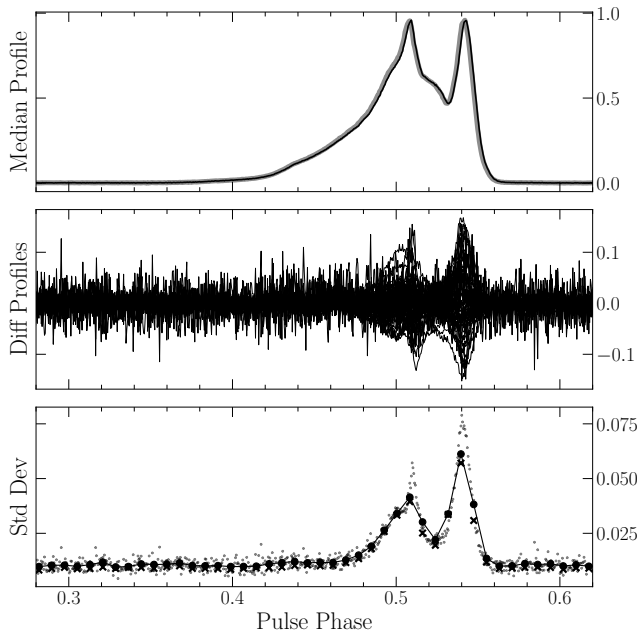


Figure 8. Profile variability visualization for 1.4 GHz data. See Figure 7’s caption for details.

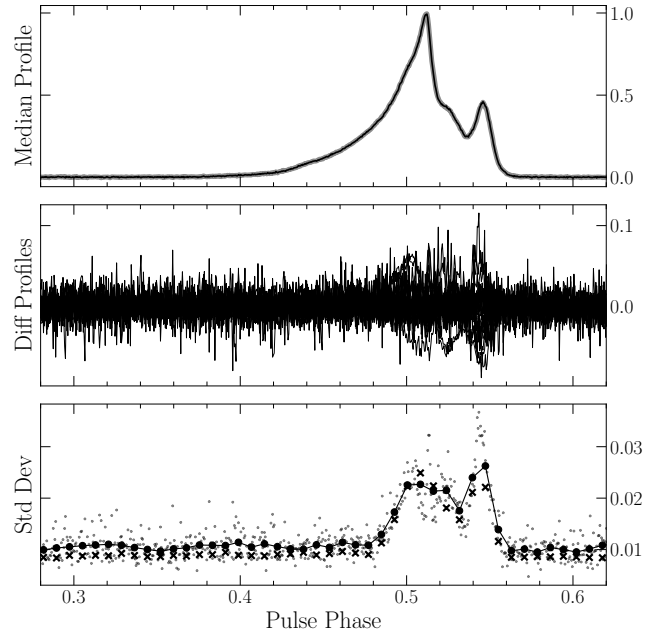


Figure 9. Profile variability visualization for 2 GHz data. See Figure 7’s caption for details.

observation having different pulse shapes, there is no consistent long-term difference.

When coupled with profile frequency evolution, interstellar scintillation could potentially cause changes in the profile shape. In our 1.4-GHz data, scintillation bandwidths range from 40–100 MHz and timescales are ~ 20 min (these are merely rough estimates based on visual inspection of our dynamic spectra). To investigate this possibility, we created profiles from 25-MHz bandwidths. For each subband, we created a comparison median profile in the same way as in the Hotan et al. (2004) method described above, so that difference profiles show the deviation from the actual pulse shape at a particular frequency, without being biased by profile frequency evolution. We found (see Figure 15 for an example) these subbanded profiles exhibited the same variability across the band within each observation, which cannot be explained by scintillation.

We also looked for variability within individual observations. For each observation at least 20 minutes long, we split the data into 5-minute subintegrations and subjected the resulting profiles to the Hotan et al. (2004) method. In most observations, comparing the subintegration profiles did not yield any signs of variability over the course of the observation itself. However, in a few cases the pulse shape did change, seemingly smoothly over a ~ 10 –15 minute timescale: see Figure 16 for an example of this. The possibility that this short-timescale variability in particular is due to scintillation

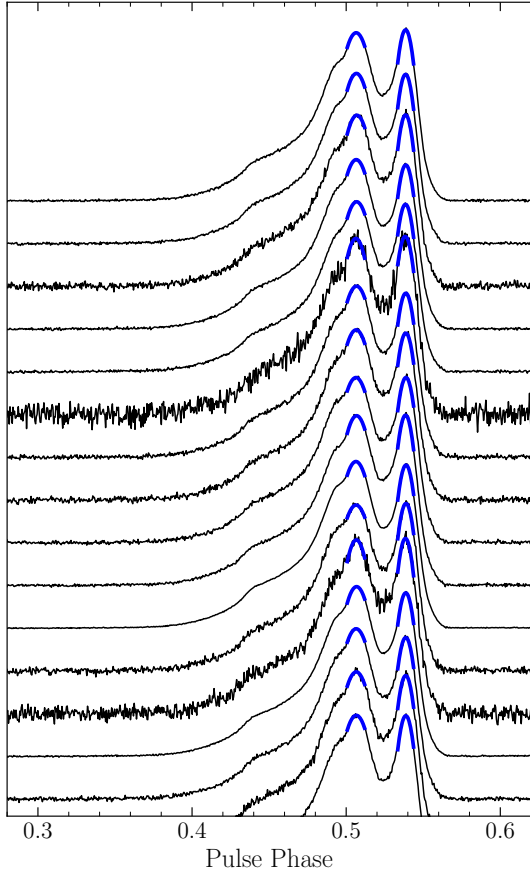


Figure 10. Best-fit parabolas (thick blue lines) used to estimate the phases and heights of the two peaks of each 430-MHz profile. The profiles are normalized such that their integrals equal the same (arbitrary) value, and they are stacked vertically simply to show each profile shape and polynomial fit.

coupled with the frequency-dependent profile shape, as mentioned above, has not been ruled out.

4.3. Timing Solution Comparison

The timing solution we obtained from the METM data set is shown in Table 3 along with the timing solution calculated from the IFA-calibrated profiles. One noticeable difference to the IFA timing solution (which has only minor differences from the NG15 solution, caused by the removal of FD parameters, as discussed in § 3.2) is the lack of a significant time derivative of the projected semimajor axis. We attribute this to the reduced S/N and fewer TOAs in the METM data set compared to the IFA data set, in which the parameter has only marginal ($3.9\text{-}\sigma$) significance. The reason for this is discussed below.

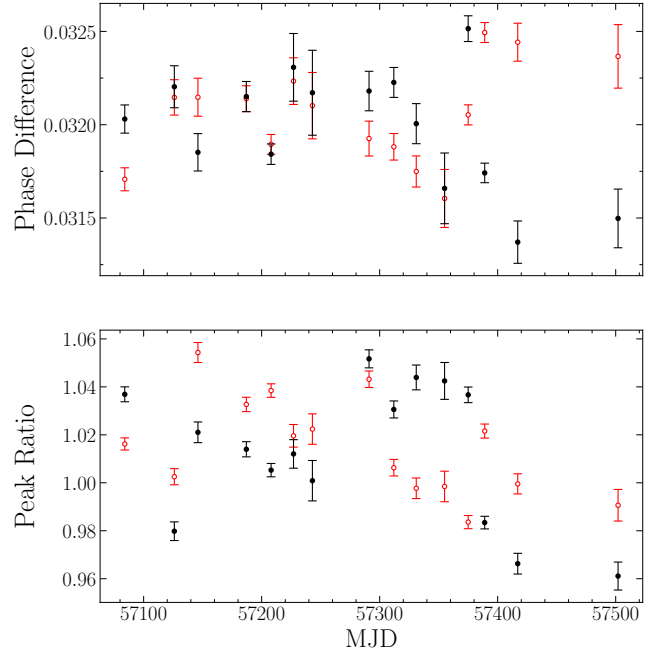


Figure 11. The results of the peak fitting method for 430 MHz data. The top panel shows differences in pulse phase between the first and second peaks. The bottom panel shows peak ratios (first peak/second peak). Each panel shows results for METM-calibrated data with filled black points, and for IFA-calibrated data with open red points. Error bars show the $1\text{-}\sigma$ uncertainties reported by the least-squares fit.

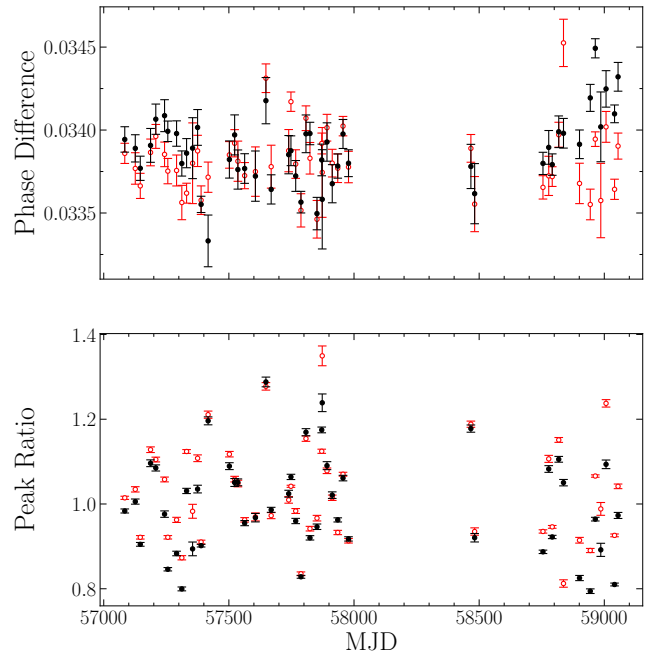


Figure 12. The results of the peak fitting method for 1.4 GHz data. See Figure 11's caption for details.

Table 3. Timing Solution and Derived Parameters for PSR J1022+1001

Parameter	METM data set	IFA data set
Timing Parameters		
Ecliptic longitude ($^{\circ}$)	153.86583002(6)	153.86583001(5)
Ecliptic latitude ($^{\circ}$)	-0.06380(6)	-0.06384(5)
Spin frequency (Hz)	60.7794488569342(4)	60.7794488570170(4)
Frequency derivative (Hz s^{-1})	$-1.6008(2) \times 10^{-16}$	$-1.6011(2) \times 10^{-16}$
Dispersion measure (pc cm^{-3})	10.263	10.266
Proper motion in lon. (mas yr^{-1})	-15.9(1)	-16.1(1)
Proper motion in lat. (mas yr^{-1})	$-2(1) \times 10^2$	$-2(1) \times 10^2$
Parallax (mas)	2.2(9)	3.0(7)
Epoch (MJD)	58048	58042
Span (MJD)	57041–59055	57028–59055
Number of TOAs	3822	3930
Epoch-averaged WRMS (μs)	3.49	3.36
Orbital Parameters		
Orbital period (days)	7.8051301610(5)	7.8051301612(4)
Projected semimajor axis (lt-s)	16.7654214(5)	16.7654227(5)
Eccentricity	$9.726(7) \times 10^{-5}$	$9.727(6) \times 10^{-5}$
Epoch of periastron (MJD)	58051.8516(8)	58044.0474(7)
Longitude of periastron ($^{\circ}$)	97.91(4)	97.95(3)
Projected semimajor axis derivative (lt-s s^{-1})	...	$3.5(9) \times 10^{-14}$
Profile Frequency-Dependence Parameters		
FD1 (μs)	$1.0(2) \times 10^{-4}$	$1.3(1) \times 10^{-4}$
FD2 (μs)	$-1.6(2) \times 10^{-4}$	$-2.0(1) \times 10^{-4}$
FD3 (μs)	$7.4(8) \times 10^{-5}$	$8.7(7) \times 10^{-5}$
Derived Parameters		
Spin period (ms)	16.4529297123745(1)	16.4529297123521(1)
Period derivative	$4.3333(5) \times 10^{-20}$	$4.3342(4) \times 10^{-20}$
Right ascension (J2000)	$10^{\text{h}} 22^{\text{m}} 57^{\text{s}} 218(5)$	$10^{\text{h}} 22^{\text{m}} 57^{\text{s}} 214(4)$
Declination (J2000)	$+10^{\circ} 01' 57'' 7(2)$	$+10^{\circ} 01' 57'' 6(2)$
Galactic longitude ($^{\circ}$)	231.79000(5)	231.79004(5)
Galactic latitude ($^{\circ}$)	51.09864(4)	51.09861(4)
Binary mass function (M_{\odot})	8.31×10^{-2}	8.31×10^{-2}
Minimum companion mass (M_{\odot})	0.72	0.72

NOTE—Numbers in parentheses are the $1\text{-}\sigma$ uncertainties in the last digit as reported by PINT. We used the DD binary timing model, DE440 Solar System Ephemeris, the TT(BIPM2021) time standard, and the IERS2010 convention for ecliptic coordinates. The minimum companion mass assumes a pulsar mass of $1.4 M_{\odot}$ and an edge-on orbit, $i = 90^{\circ}$. Not shown are the two fitted JUMP parameters, which account for the phase offsets between the three receivers at AO; and the 54/55 DMX parameters, for which the reported DMs are reference values.

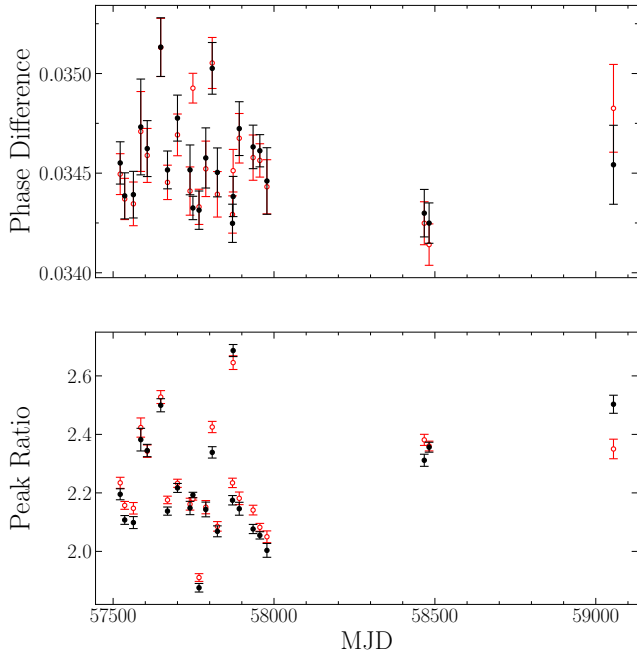


Figure 13. The results of the peak fitting method for 2 GHz data. See Figure 11’s caption for details.

Table 4 shows various metrics of evaluating the suitability of both data sets’ timing solutions. For 430 MHz data, the METM method causes a significant improvement in each RMS value. Notably, there are only 158 TOAs at 430 MHz in the METM data set, vs. 219 in the IFA data set. Differences in the number of TOAs, and S/N, result from frequency channels being eliminated due to RFI in the observations of PSRs B0525+21, B1937+21, or J0030+0451 (or the corresponding noise diode observations), or `pcm` failing to achieve a solution for the PR in certain frequency channels. In these ways, polarization calibration can corrupt frequency channels, leading to fewer (in the cases where subbands are eliminated altogether) or lower-S/N (when a limited number of frequency channels are corrupted within a subband) TOAs.

For 1.4 and 2 GHz data, which have many more TOAs than the 430 MHz data, IFA leads to a better timing solution than METM by every metric. Therefore, it would seem that calibrating NANOGrav observations using METM generally does not lead to an improvement in the timing solution over the standard IFA method.

5. SUMMARY & DISCUSSION

PSR J1022+1001’s pulse profile exhibits significant variability in the NANOGrav 15-yr data set, in data taken from 430 MHz to 2 GHz. We have applied a robust polarization calibration scheme to these data and see no increased stability as a result. These results agree

with those of Kramer et al. (1999) and Padmanabh et al. (2021), and run counter to Hotan et al. (2004), in finding significant pulse profile variability that does not appear to be caused by incorrect polarization calibration.

Our polarization calibration scheme does not lead to an overall improvement in the quality of the timing solution obtained from the data. In fact, data that only underwent a standard polarization calibration procedure have a slightly higher-quality fit. These results are consistent with a parallel study that more thoroughly compares NANOGrav timing results between different polarization calibration methods using data from the Green Bank Telescope (Dey et al. 2024). We may therefore tentatively conclude that incorrect polarization calibration is not responsible for the pulse profile changes observed, though it is of course possible that yet more accurate polarization calibration could be explored.

Because the pulse profiles obtained using narrower bandwidths are variable in the same way as frequency-averaged profiles, a potential cause in the combination of profile frequency-dependence and interstellar scintillation, as proposed by Shao & You (2016), is ruled out. This leaves mechanisms intrinsic to the pulsar as the most likely cause of the variability. As discussed in §1, these mechanisms include pulse-to-pulse jitter, precession, and mode-changing. The long timescale of the variations is inconsistent with jitter, and the seemingly random variations on long (months to years) timescales are inconsistent with expectations for precession. Single pulse studies have not indicated that PSR J1022+1001 exhibits nulling, mode-changing, or giant pulses, and measurements of jitter noise have been inconsistent (Shao & You 2016; Palliyaguru et al. 2021; Feng et al. 2021).

While our observed pulse shapes do not appear to fall into a number of discrete modes, it is possible that modeling the pulse shape as linear combinations of averages of the most extreme peak-ratio profiles could lead to evidence of mode-changing, as it did for PSR B1828–11 (Stairs et al. 2019). Aside from mode-changing, which merits further investigation along the lines of PSR B1828–11, the explanation for the observed variability that remains is some phenomenon in the pulsar magnetosphere, such as those proposed by Ramachandran & Kramer (2003) and Liu et al. (2015).

PSR J1022+1001 has respectable timing precision despite its variable pulse shape: its epoch-averaged rms residual in the NANOGrav 15-yr data set is about $3 \mu\text{s}$. One potential way to improve precision further is by accounting for the variability with a TOA generation method that allows pulse shapes to vary. While such methods have been demonstrated (Kramer et al. 1999;

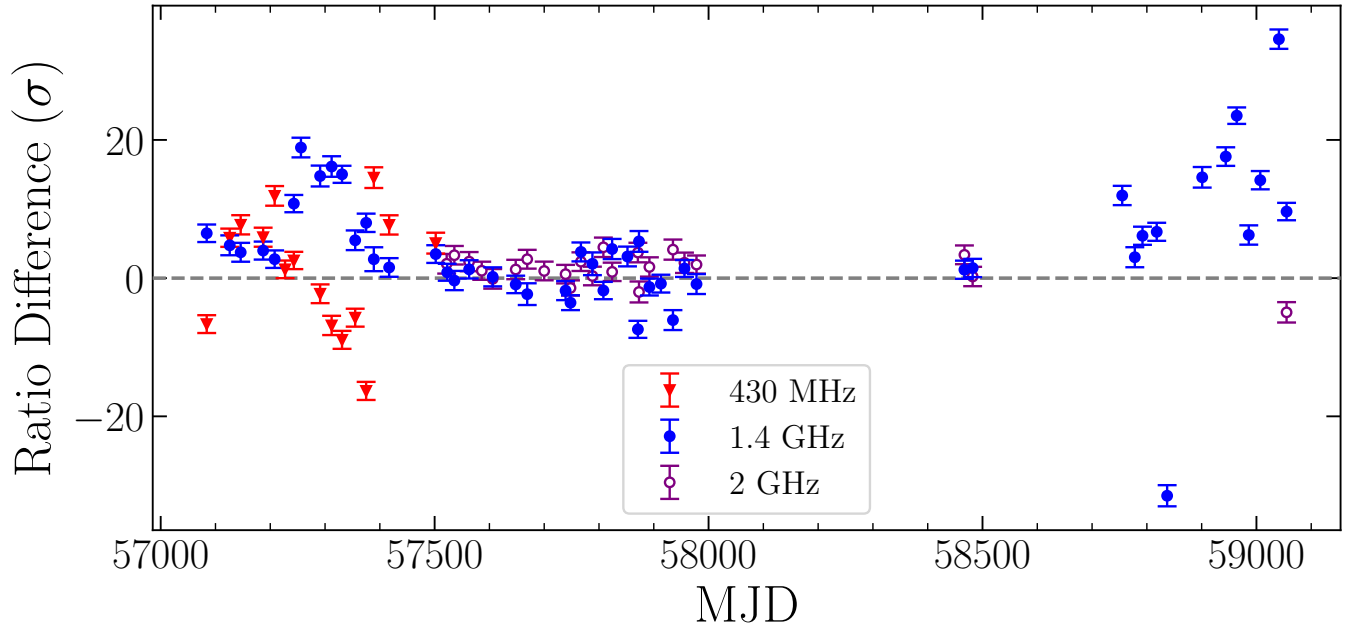


Figure 14. Each point, representing a single observation, shows the difference between the peak ratio obtained from IFA- and METM-calibrated data (i.e. corresponding red and black points from the bottom panels of figures 11, 12, and 13), in terms of the $1\text{-}\sigma$ uncertainty on the METM-calibrated peak ratio. Red triangles are 430-MHz data, filled blue circles are 1.4 GHz, and empty purple circles are 2 GHz. The dashed gray line denotes equal peak ratios.

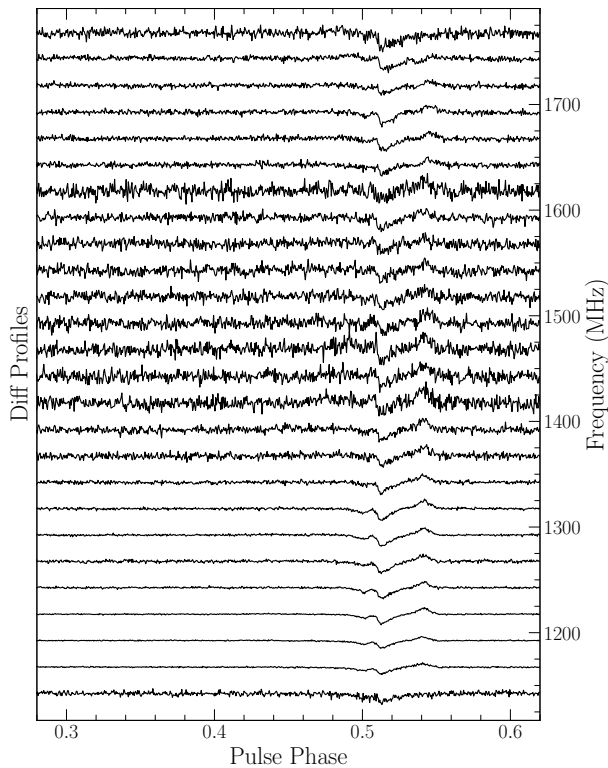


Figure 15. Example deviations from the median pulse shape in each 25-MHz subband, from a 1.4-GHz observation on 24 April 2016 (MJD 57502).

Shannon & Cordes 2012), applying one in a PTA context would require careful consideration, and is beyond the scope of this analysis.

AUTHOR CONTRIBUTIONS

W.F. performed the analysis and prepared the text, figures, and tables. M.A.M. provided valuable guidance and feedback over the course of the project. The polarization calibration procedure was based on previous work by P.A.G. and H.M.W., and was further refined by W.F. and L.D. K.C. and I.H.S. ran the observations of PSR B0525+21. G.A., A.A., A.M.A., Z.A., P.T.B., P.R.B., H.T.C., K.C., M.E.D., P.B.D., T.D., E.C.F., W.F., E.F., G.E.F., N.G.D., P.A.G., J.G., D.C.G., J.S.H., R.J.J., M.L.J., D.L.K., M.K., M.T.L., D.R.L., J.L., R.S.L., A.M., M.A.M., N.M., B.W.M., C.N., D.J.N., T.T.P., B.B.P.P., N.S.P., H.A.R., S.M.R., P.S.R., A.S., C.S., B.J.S., I.H.S., K.S., A.S., J.K.S., and H.M.W. developed the NANOGrav 15-yr data set through a combination of observations, data reduction, code development, timing analysis, and other contributions detailed in Agazie et al. (2023b).

ACKNOWLEDGEMENTS

Table 4. Timing Analysis Comparison

Rcvr	Method	N_{TOA}	S/N_{med}	RMS_{all}	RMS_{avg}	WRMS_{all}	WRMS_{avg}	EFAC
				(μs)	(μs)	(μs)	(μs)	
All	IFA	3930	148.5	4.53	6.37	2.68	3.36	...
	METM	3822	143.8	3.79	7.25	2.81	3.49	...
430	IFA	219	251.4	9.90	11.47	9.91	10.07	1.26
	METM	158	249.8	4.94	8.03	4.96	6.51	1.30
L-wide	IFA	2559	163.2	2.17	5.33	2.19	2.91	1.07
	METM	2555	161.8	2.24	5.67	2.26	3.01	1.14
S-wide	IFA	1152	115.2	3.33	7.08	3.27	4.40	1.14
	METM	1109	101.0	4.91	9.90	4.85	5.19	1.29

NOTE—Timing analysis comparison between the IFA and METM data sets. Columns report the number of TOAs (N_{TOA}), median TOA S/N (S/N_{med}), unweighted (RMS) and weighted (WRMS) root mean square of all or epoch-averaged TOAs. The first set of two rows shows results for all combined data, and subsequent rows show results for data from individual receivers, as well as the EFAC white noise parameter for each receiver.

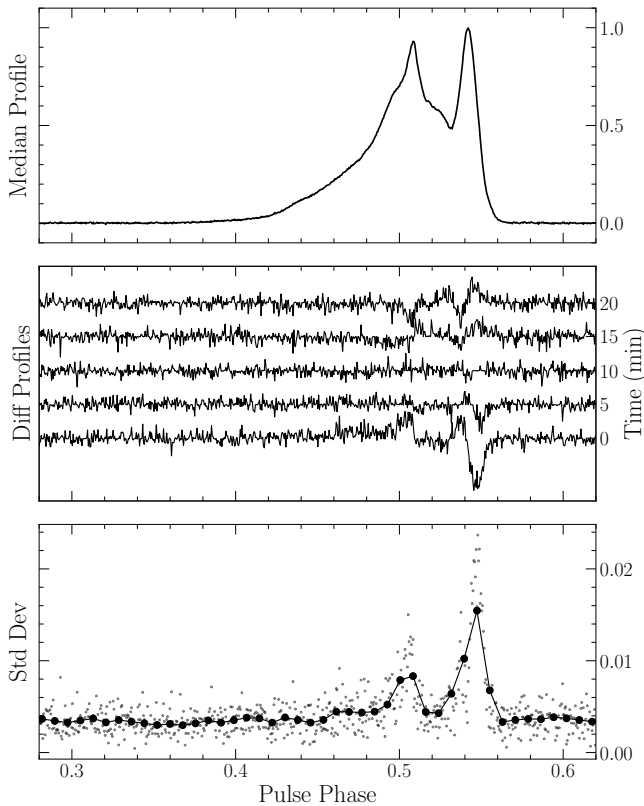


Figure 16. Example of an observation that shows changing variability between 5-minute subintegrations. The middle panel shows a difference profile from each subintegration: the data minus the median profile, which is shown in the top panel. The bottom panel shows the binned standard deviations in the same manner as in Figure 7. Data are from a 1.4-GHz observation made on 3 March 2015 (MJD 57084).

The authors thank Loren Anderson, who, along with M.A.M., D.L.K., and D.R.L., gave valuable comments on this paper as part of reviewing W.F.’s Ph.D. thesis.

The NANOGrav Collaboration receives support from National Science Foundation (NSF) Physics Frontiers Center award Nos. 1430284 and 2020265, the Gordon and Betty Moore Foundation, NSF AccelNet award No. 2114721, an NSERC Discovery Grant, and CIFAR. The Arecibo Observatory is a facility of the NSF operated under cooperative agreement (AST-1744119) by the University of Central Florida (UCF) in alliance with Universidad Ana G. Méndez (UAGM) and Yang Enterprises (YEI), Inc.

M.A.M. is supported by NSF #2009425. M.A.M. and D.R.L. are supported by NSF #1458952. P.R.B. is supported by the Science and Technology Facilities Council, grant number ST/W00946/1. Pulsar research at UBC is supported by an NSERC Discovery Grant and by CIFAR. K.C. is supported by a UBC Four Year Fellowship (6456). M.E.D. acknowledges support from the Naval Research Laboratory by NASA under contract S-15633Y. L.D. is supported by a WVU postdoctoral fellowship. T.D. and M.T.L. are supported by an NSF Astronomy and Astrophysics Grant (AAG) award number 2009468. E.C.F. is supported by NASA under award number 80GSFC21M0002. G.E.F. is supported by NSF award PHY-2011772. The Dunlap Institute is funded by an endowment established by the David Dunlap family and the University of Toronto. T.T.P. acknowledges support from the Extragalactic Astrophysics Research Group at Eötvös Loránd University, funded by the Eötvös Loránd Research Network (ELKH), which was used during the development of this research. N.S.P.

was supported by the Vanderbilt Initiative in Data Intensive Astrophysics (VIDA) Fellowship. H.A.R. is supported by NSF Partnerships for Research and Education in Physics (PREP) award No. 2216793. S.M.R. and I.H.S. are CIFAR Fellows. Portions of this work performed at NRL were supported by ONR 6.1 basic research funding.

Facilities: AO (PUPPI)

Software: `astropy` (Astropy Collaboration et al. 2022), `ENTERPRISE` (Ellis et al. 2020), `ionFR` (Sotomayor-Beltran et al. 2013), `matplotlib` (Hunter 2007), `numpy` (Harris et al. 2020), `PINT` (Luo et al. 2021; Susobhanan et al. 2024), `PSRCHIVE` (van Straten et al. 2011), `scipy` (Virtanen et al. 2020)

REFERENCES

- Agazie, G., Anumarlapudi, A., Archibald, A. M., et al. 2023a, *ApJL*, 951, L8, doi: [10.3847/2041-8213/acdac6](https://doi.org/10.3847/2041-8213/acdac6)
- Agazie, G., Alam, M. F., Anumarlapudi, A., et al. 2023b, *ApJL*, 951, L9, doi: [10.3847/2041-8213/acda9a](https://doi.org/10.3847/2041-8213/acda9a)
- Agazie, G., Anumarlapudi, A., Archibald, A. M., et al. 2023c, *ApJL*, 951, L10, doi: [10.3847/2041-8213/acda88](https://doi.org/10.3847/2041-8213/acda88)
- Alam, M. F., Arzoumanian, Z., Baker, P. T., et al. 2021, *ApJS*, 252, 4, doi: [10.3847/1538-4365/abc6a0](https://doi.org/10.3847/1538-4365/abc6a0)
- Antoniadis, J., Arumugam, P., Arumugam, S., et al. 2023a, arXiv e-prints, arXiv:2306.16214, doi: [10.48550/arXiv.2306.16214](https://doi.org/10.48550/arXiv.2306.16214)
- Antoniadis, J., Babak, S., Bak Nielsen, A. S., et al. 2023b, arXiv e-prints, arXiv:2306.16224, doi: [10.48550/arXiv.2306.16224](https://doi.org/10.48550/arXiv.2306.16224)
- Astropy Collaboration, Price-Whelan, A. M., Lim, P. L., et al. 2022, *ApJ*, 935, 167, doi: [10.3847/1538-4357/ac7c74](https://doi.org/10.3847/1538-4357/ac7c74)
- Backer, D. C. 1970, *Nature*, 228, 1297, doi: [10.1038/2281297a0](https://doi.org/10.1038/2281297a0)
- Britton, M. C. 2000, *ApJ*, 532, 1240, doi: [10.1086/308595](https://doi.org/10.1086/308595)
- Cameron, A. D., Bailes, M., Champion, D. J., et al. 2023, *MNRAS*, 523, 5064, doi: [10.1093/mnras/stad1712](https://doi.org/10.1093/mnras/stad1712)
- Camilo, F., Nice, D. J., Shrauner, J. A., & Taylor, J. H. 1996, *ApJ*, 469, 819, doi: [10.1086/177829](https://doi.org/10.1086/177829)
- Damour, T., & Deruelle, N. 1985, *Annales de L'Institut Henri Poincare Section (A) Physique Theorique*, 43, 107
- Dey, L., McLaughlin, M. A., Wahl, H. M., et al. 2024, arXiv e-prints, arXiv:2406.13463, <https://arxiv.org/abs/2406.13463>
- Ellis, J. A., Vallisneri, M., Taylor, S. R., & Baker, P. T. 2020, *ENTERPRISE: Enhanced Numerical Toolbox Enabling a Robust Pulsar Inference Suite*, Zenodo, doi: [10.5281/zenodo.4059815](https://doi.org/10.5281/zenodo.4059815)
- Everett, J. E., & Weisberg, J. M. 2001, *ApJ*, 553, 341, doi: [10.1086/320652](https://doi.org/10.1086/320652)
- Feng, Y., Hobbs, G., Li, D., et al. 2021, *ApJ*, 908, 105, doi: [10.3847/1538-4357/abd326](https://doi.org/10.3847/1538-4357/abd326)
- Foster, R. S., & Backer, D. C. 1990, *ApJ*, 361, 300, doi: [10.1086/169195](https://doi.org/10.1086/169195)
- Gentile, P. A., McLaughlin, M. A., Demorest, P. B., et al. 2018, *ApJ*, 862, 47, doi: [10.3847/1538-4357/aac9c9](https://doi.org/10.3847/1538-4357/aac9c9)
- Hamaker, J. P. 2000, *A&AS*, 143, 515, doi: [10.1051/aas:2000337](https://doi.org/10.1051/aas:2000337)
- Harris, C. R., Millman, K. J., van der Walt, S. J., et al. 2020, *Nature*, 585, 357, doi: [10.1038/s41586-020-2649-2](https://doi.org/10.1038/s41586-020-2649-2)
- Heiles, C., Perillat, P., Nolan, M., et al. 2001, *PASP*, 113, 1274, doi: [10.1086/323289](https://doi.org/10.1086/323289)
- Hotan, A. W., Bailes, M., & Ord, S. M. 2004, *MNRAS*, 355, 941, doi: [10.1111/j.1365-2966.2004.08376.x](https://doi.org/10.1111/j.1365-2966.2004.08376.x)
- Hunter, J. D. 2007, *Computing in Science & Engineering*, 9, 90, doi: [10.1109/MCSE.2007.55](https://doi.org/10.1109/MCSE.2007.55)
- Jennings, R. J., Cordes, J. M., Chatterjee, S., et al. 2024, *ApJ*, 964, 179, doi: [10.3847/1538-4357/ad2930](https://doi.org/10.3847/1538-4357/ad2930)
- Jones, M. L., McLaughlin, M. A., Lam, M. T., et al. 2017, *ApJ*, 841, 125, doi: [10.3847/1538-4357/aa73df](https://doi.org/10.3847/1538-4357/aa73df)
- Kramer, M., Xilouris, K. M., Camilo, F., et al. 1999, *ApJ*, 520, 324, doi: [10.1086/307449](https://doi.org/10.1086/307449)
- Lam, M. T., McLaughlin, M. A., Arzoumanian, Z., et al. 2019, *ApJ*, 872, 193, doi: [10.3847/1538-4357/ab01cd](https://doi.org/10.3847/1538-4357/ab01cd)
- Liu, K., Karuppusamy, R., Lee, K. J., et al. 2015, *MNRAS*, 449, 1158, doi: [10.1093/mnras/stv397](https://doi.org/10.1093/mnras/stv397)
- Lorimer, D. R., & Kramer, M. 2004, *Handbook of Pulsar Astronomy* (UK: Cambridge University Press)
- Luo, J., Ransom, S., Demorest, P., et al. 2021, *ApJ*, 911, 45, doi: [10.3847/1538-4357/abe62f](https://doi.org/10.3847/1538-4357/abe62f)
- NANOGrav Collaboration, Arzoumanian, Z., Brazier, A., et al. 2015, *ApJ*, 813, 65, doi: [10.1088/0004-637X/813/1/65](https://doi.org/10.1088/0004-637X/813/1/65)
- Padmanabh, P. V., Barr, E. D., Champion, D. J., et al. 2021, *MNRAS*, 500, 1178, doi: [10.1093/mnras/staa3174](https://doi.org/10.1093/mnras/staa3174)
- Palliyaguru, N. T., Perera, B. B. P., McLaughlin, M. A., Osłowski, S., & Siebert, G. L. 2021, arXiv e-prints, arXiv:2201.00624, doi: [10.48550/arXiv.2201.00624](https://doi.org/10.48550/arXiv.2201.00624)
- Radhakrishnan, V., & Cooke, D. J. 1969, *Astrophys. Lett.*, 3, 225
- Ramachandran, R., & Kramer, M. 2003, *A&A*, 407, 1085, doi: [10.1051/0004-6361:20031036](https://doi.org/10.1051/0004-6361:20031036)
- Ransom, S., Brazier, A., Chatterjee, S., et al. 2019, in *Bulletin of the American Astronomical Society*, Vol. 51, 195, doi: [10.48550/arXiv.1908.05356](https://doi.org/10.48550/arXiv.1908.05356)

- Ransom, S. M., Demorest, P., Ford, J., et al. 2009, in American Astronomical Society Meeting Abstracts, Vol. 214, American Astronomical Society Meeting Abstracts #214, 605.08
- Reardon, D. J., Zic, A., Shannon, R. M., et al. 2023, *ApJL*, 951, L6, doi: [10.3847/2041-8213/acdd02](https://doi.org/10.3847/2041-8213/acdd02)
- Shannon, R. M., & Cordes, J. M. 2012, *ApJ*, 761, 64, doi: [10.1088/0004-637X/761/1/64](https://doi.org/10.1088/0004-637X/761/1/64)
- Shao, M., & You, X. P. 2016, *Acta Astronomica Sinica*, 57, 517
- Sotomayor-Beltran, C., Sobey, C., Hessels, J. W. T., et al. 2013, *A&A*, 552, A58, doi: [10.1051/0004-6361/201220728](https://doi.org/10.1051/0004-6361/201220728)
- Stairs, I. H., Thorsett, S. E., & Camilo, F. 1999, *ApJS*, 123, 627, doi: [10.1086/313245](https://doi.org/10.1086/313245)
- Stairs, I. H., Lyne, A. G., Kramer, M., et al. 2019, *MNRAS*, 485, 3230, doi: [10.1093/mnras/stz647](https://doi.org/10.1093/mnras/stz647)
- Susobhanan, A., Kaplan, D., Archibald, A., et al. 2024, arXiv e-prints, arXiv:2405.01977, doi: [10.48550/arXiv.2405.01977](https://doi.org/10.48550/arXiv.2405.01977)
- Taylor, J. H. 1992, *Philosophical Transactions of the Royal Society of London Series A*, 341, 117, doi: [10.1098/rsta.1992.0088](https://doi.org/10.1098/rsta.1992.0088)
- Van Rooy, P., Whitlow, D., & Seymour, A. 2017, in American Astronomical Society Meeting Abstracts, Vol. 229, American Astronomical Society Meeting Abstracts #229, 137.05
- van Straten, W. 2002, *ApJ*, 568, 436, doi: [10.1086/338810](https://doi.org/10.1086/338810)
- . 2004, *ApJS*, 152, 129, doi: [10.1086/383187](https://doi.org/10.1086/383187)
- . 2013, *ApJS*, 204, 13, doi: [10.1088/0067-0049/204/1/13](https://doi.org/10.1088/0067-0049/204/1/13)
- van Straten, W., Demorest, P., Khoo, J., et al. 2011, PSRCHIVE: Development Library for the Analysis of Pulsar Astronomical Data, Astrophysics Source Code Library, record ascl:1105.014. <http://ascl.net/1105.014>
- Virtanen, P., Gommers, R., Oliphant, T. E., et al. 2020, *Nature Methods*, 17, 261, doi: [10.1038/s41592-019-0686-2](https://doi.org/10.1038/s41592-019-0686-2)
- Wahl, H. M., McLaughlin, M. A., Gentile, P. A., et al. 2022, *ApJ*, 926, 168, doi: [10.3847/1538-4357/ac4045](https://doi.org/10.3847/1538-4357/ac4045)
- Wang, N., Manchester, R. N., & Johnston, S. 2007, *MNRAS*, 377, 1383, doi: [10.1111/j.1365-2966.2007.11703.x](https://doi.org/10.1111/j.1365-2966.2007.11703.x)
- Xu, H., Chen, S., Guo, Y., et al. 2023, *Research in Astronomy and Astrophysics*, 23, 075024, doi: [10.1088/1674-4527/acdfa5](https://doi.org/10.1088/1674-4527/acdfa5)
- Zic, A., Reardon, D. J., Kapur, A., et al. 2023, arXiv e-prints, arXiv:2306.16230, doi: [10.48550/arXiv.2306.16230](https://doi.org/10.48550/arXiv.2306.16230)